



Modelling and dynamical analysis of a DC–DC converter with coupled inductors

María Belén D'Amico¹ · Sergio A. González²

Received: 8 March 2018 / Accepted: 14 February 2019 / Published online: 27 February 2019
© Springer-Verlag GmbH Germany, part of Springer Nature 2019

Abstract

The large-signal averaged model of a coupled-inductor double-boost converter is developed and analysed in this paper. Due to the large current fluctuations, the differential system is deduced by averaging the circuit equations of the operation modes over a switching period. Generic expressions that permit to calculate the current commutation intervals as function of the averaged state variables are also found to complete the model. Resistive losses are introduced into an equivalent averaged circuit leading to a more realistic scenario. The proposed state-space model is used for studying voltage conversion ratios, transients and frequency-domain responses of the converter as well as for designing a control loop that regulates the output voltage. Numerical simulations and experimental measurements corroborate the obtained results.

Keywords DC–DC converter · High conversion ratio · Averaged model · Dynamical behaviour

1 Introduction

Non-isolated high step-up DC–DC converters play an important role in many applications related to sustainable energy systems, electric and fuel cell vehicles, power supplies, among others. In general, high efficiencies, reduced number of components and conversion ratios above ten are desired. To fulfil these specifications, different topologies have been proposed [1,2]. High boost capacities are achieved, for example, connecting classical configurations in cascade, adding magnetic coupling between inductors, using clamping stages and, also, combining more than one of these alternatives [3–7]. In particular, the coupled-inductor double-boost converter (CBC) derives from the cascade connection of two boost converters where inductors are coupled magnetically replacing the switch of the second stage [8]. Other simple and non-isolated circuits based on two coupled inductors and a

single switch can be found in [9–12]. In low-power applications, these topologies are easily implemented and they have a reduced cost.

The design and understanding of the CBC presuppose the development of an adequate model. As other high step-up converters, the complete dynamics of the CBC can be represented by switching successively the electrical equations that describe the operation modes of the circuit. On the other hand, the average behaviour of the system can be obtained by averaging the switching component waveforms (circuit averaging) or the state variables equations (state-space averaging) over a switching period [13,14]. The circuit-averaging technique leads commonly to small-signal models (see, for instance, [15,16]). The state-space averaging technique produces naturally continuous and nonlinear differential systems. As widely known, averaged models are an accessible tool for dynamical analysis as well as control design.

If the states do not change significantly from their mean values, the averaged state-space model of a converter can be derived by averaging the matrices associated with its operation modes [17,18]. Due to the magnetic coupling of the CBC, the inductor currents commute during two intervals and, even, they become zero even though the flux is continuous. Because of the large current fluctuations, the response of that model presents considerable differences with respect to the actual behaviour of the circuit. A procedure for improving

✉ María Belén D'Amico
mbdamico@uns.edu.ar

Sergio A. González
sag@ing.unlp.edu.ar

¹ Instituto de Inv. en Ing. Eléctrica (UNS - CONICET),
Dept. de Ingeniería Eléctrica y de Computadoras, Universidad
Nacional del Sur, San Andrés 800, Bahía Blanca, Argentina

² Instituto LEICI (UNLP-CONICET), Dept. de Electrotecnia,
Facultad de Ingeniería, Universidad Nacional de La Plata,
La Plata, Argentina

the averaged matrices is proposed in [19,20] and then used in [21] for obtaining the analytical model of a coupled-inductor boost converter. Due to the simplicity of that topology, an artificial current proportional to the magnetic flux is defined, reducing the states of the differential system. Moreover, a perfect magnetic coupling is considered, neglecting an operation mode of the circuit. For converters like the CBC, the aforementioned simplifications cannot be applied and then, the procedure implies the realization of cumbersome simulations to correct the matrices numerically for an specific operating range.

In this paper, the averaged state-space model of the CBC is deduced analytically by averaging the circuit equations over a switching period [22]. The differential system contains the four physical state-space variables of the converter, and the coupling factor is lower than unity to replicate its actual operation principle. These facts lead to a more meticulous treatment of the averaging integrals and algebraic developments for obtaining the expressions of the commutation intervals. The analytical model is first deduced without considering the losses of the components. The differential system follows appropriately temporal and frequency-domain responses of the simulated converter. The obtained results present significant improvements compared to the preliminary contribution [23] where a small-signal model of the CBC was derived by making strong simplifications on the current commutation intervals.

Parasitic resistances representing the losses of components and semiconductors are also introduced to the model. To handle them in a simple way, an equivalent averaged circuit is derived. As corroborated by experimental measurements, the proposed model can reproduce correctly the average of the physical states of the CBC. Furthermore, it is demonstrated to be useful for analysing the dependency of the conversion ratios and dynamical responses on the magnetic coupling and resistive losses. The obtained information permits to design a control loop that regulates adequately the output voltage under load perturbations.

This paper is organized as follows. In Sect. 2, the topology and operation of the CBC are briefly described. Developments concerning the averaged state-space modelling of the converter are presented in Sect. 3. Results provided by that model are analysed in Sect. 4. Resistive parasitics are treated in Sect. 5. In Sect. 6, the responses of the newly proposed model are contrasted with experimental measurements. Finally, conclusions are given in Sect. 7.

2 Topology description

The topology of the CBC is shown in Fig. 1, which can be seen as a cascade of two boost converters: the first one composed of L_1 , C_1 and diode D_1 and the second one composed

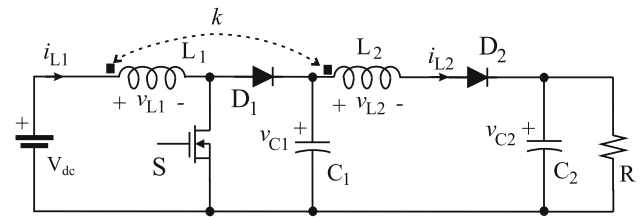


Fig. 1 Coupled-inductor double-boost converter

of L_2 , C_2 and diode D_2 . There only exists an active switch S , which is controlled by a PWM signal of fixed period T and duty cycle d . The switch of the second boost is replaced by the magnetic coupling between inductors L_1 and L_2 [8].

In the following, it is considered that:

- switch S and diodes D_1 and D_2 are ideal;
- the magnetic flux in L_1 and L_2 is continuous;
- the coupling between L_1 and L_2 is not perfect.

Under these assumptions, the induced voltages in the inductors are given by the mutual inductance $M = k\sqrt{L_1 L_2}$ with factor k less than 1. Thus,

$$\begin{aligned} v_{L1} &= L_1 \frac{di_{L1}}{dt} + M \frac{di_{L2}}{dt}, \\ v_{L2} &= L_2 \frac{di_{L2}}{dt} + M \frac{di_{L1}}{dt}. \end{aligned} \quad (1)$$

Moreover, the converter operates into four different modes during a switching period T [8]. The waveforms presented by currents i_{L1} and i_{L2} and voltages v_{C1} and v_{C2} are illustrated in Fig. 2. The two intervals for which both currents are different from zero simultaneously are represented as d_1 and d_2 .

- *Mode 1* ($0 - d_1 T$): Switch S is turned on and diode D_2 is forward-biased. So, current from L_2 commutes to L_1 until $i_{L2} = 0$.
- *Mode 2* ($d_1 T - d T$): Switch S is still turned on but diode D_2 is reversed-biased. So, inductor L_1 is charged by the input source V_{dc} and the load R is supplied by C_2 .
- *Mode 3* ($d T - (d + d_2) T$): Switch S is turned off and diodes D_1 and D_2 are forward-biased. So, current in L_1 commutes to L_2 until $i_{L1} = 0$.
- *Mode 4* ($(d + d_2) T - T$): Switch S is turned off and diode D_1 is reversed-biased. So, part of the energy storage by L_2 charges C_2 and it also supplies R .

Taking into account (1) and applying Kirchhoff laws to the circuit of Fig. 1 for each operation mode, differential equations describing the evolution of the states of the converter are obtained. They are resumed in Table 1 where vector $x = [i_{L1}, i_{L2}, v_{C1}, v_{C2}]^T$.

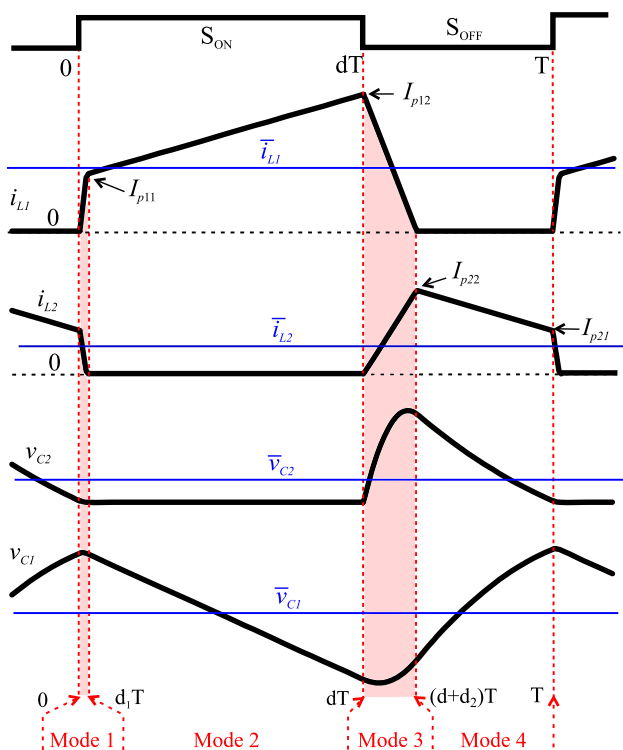


Fig. 2 Waveforms of currents and voltages during one switching period. Averaged levels are indicated with thin solid lines. Shaded zones correspond to current commutation intervals

In the following section, a state-space model that permits to infer the average dynamics of the currents and voltages is obtained, providing an appropriate perception into the behaviour of the converter.

Table 1 Circuit equations of the CBC for each operation mode

Mode 1	$\dot{x} = A_1x + B_1V_{dc}$	With	$A_1 = \begin{bmatrix} 0 & 0 & -\frac{M}{L_1L_2-M^2} & \frac{M}{L_1L_2-M^2} \\ 0 & 0 & \frac{L_1}{L_1L_2-M^2} & -\frac{L_1}{L_1L_2-M^2} \\ 0 & -\frac{1}{C_1} & 0 & 0 \\ 0 & \frac{1}{C_2} & 0 & -\frac{1}{C_2R} \end{bmatrix}; B_1 = \begin{bmatrix} \frac{L_2}{L_1L_2-M^2} \\ -\frac{M}{L_1L_2-M^2} \\ 0 \\ 0 \end{bmatrix}$
Mode 2	$\dot{x} = A_2x + B_2V_{dc}$	With	$A_2 = \begin{bmatrix} 0 & 0 & 0 & 0 \\ 0 & 0 & 0 & 0 \\ 0 & 0 & 0 & 0 \\ 0 & 0 & 0 & -\frac{1}{C_2R} \end{bmatrix}; B_2 = \begin{bmatrix} \frac{1}{L_1} \\ 0 \\ 0 \\ 0 \end{bmatrix}$
Mode 3	$\dot{x} = A_3x + B_3V_{dc}$	With	$A_3 = \begin{bmatrix} 0 & 0 & -\frac{L_2+M}{L_1L_2-M^2} & \frac{M}{L_1L_2-M^2} \\ 0 & 0 & \frac{L_1+M}{L_1L_2-M^2} & -\frac{L_1}{L_1L_2-M^2} \\ \frac{1}{C_1} & -\frac{1}{C_1} & 0 & 0 \\ 0 & \frac{1}{C_2} & 0 & -\frac{1}{C_2R} \end{bmatrix}; B_3 = \begin{bmatrix} \frac{L_2}{L_1L_2-M^2} \\ -\frac{M}{L_1L_2-M^2} \\ 0 \\ 0 \end{bmatrix}$
Mode 4	$\dot{x} = A_4x + B_4V_{dc}$	With	$A_4 = \begin{bmatrix} 0 & 0 & 0 & 0 \\ 0 & 0 & \frac{1}{L_2} & -\frac{1}{L_2} \\ 0 & -\frac{1}{C_1} & 0 & 0 \\ 0 & \frac{1}{C_2} & 0 & -\frac{1}{C_2R} \end{bmatrix}; B_4 = \begin{bmatrix} 0 \\ 0 \\ 0 \\ 0 \end{bmatrix}$

In the expressions, $x = [i_{L1}, i_{L2}, v_{C1}, v_{C2}]^T$

3 Averaged modelling

From an averaged modelling perspective, the CBC presents a particular scenario due to the existence of intervals for which inductor currents are equal to zero (Fig. 2). Even though it is still possible to assume that the ripple in capacitor voltages is very small, the same does not apply to the currents. They deviate significantly from their average values causing that the average of products $A_i x$ ($i = 1, \dots, 4$) over a switching period is not equal to the product of the averages [13]. Thus, the well-known averaged model

$$\dot{\bar{x}} = \bar{A}\bar{x} + \bar{B}V_{dc}$$

with \bar{x} as the average of x and

$$\begin{aligned} \bar{A} &= d_1A_1 + (d - d_1)A_2 + d_2A_3 + (1 - d - d_2)A_4, \\ \bar{B} &= d_1B_1 + (d - d_1)B_2 + d_2B_3 + (1 - d - d_2)B_4, \end{aligned}$$

predicts dynamical behaviours with substantial differences with respect to real ones.

To obtain an adequate model of the CBC, averaging formula

$$\dot{\bar{x}} = \frac{1}{T} \int_0^T \dot{x}(\tau) d\tau, \tag{2}$$

is applied formally on Kirchhoff equations [22]. Taking into account the expressions derived from the matrix structure in

Table 1, calculations are given by

$$\begin{aligned}
 \frac{di_{L1}}{dt} &= \frac{1}{T} \int_0^{d_1 T} \frac{-Mv_{C1} + Mv_{C2} + L_2 V_{dc}}{L_1 L_2 - M^2} dt \\
 &\quad + \frac{1}{T} \int_{d_1 T}^{dT} \frac{V_{dc}}{L_1} dt \\
 &\quad + \frac{1}{T} \int_{dT}^{(d+d_2)T} \frac{-(L_2 + M)v_{C1} + Mv_{C2} + L_2 V_{dc}}{L_1 L_2 - M^2} dt \\
 \frac{di_{L2}}{dt} &= \frac{1}{T} \int_0^{d_1 T} \frac{L_1 v_{C1} - L_1 M v_{C2} - M V_{dc}}{L_1 L_2 - M^2} dt \\
 &\quad + \frac{1}{T} \int_{dT}^{(d+d_2)T} \frac{(L_1 + M)v_{C1} - L_1 v_{C2} - M V_{dc}}{L_1 L_2 - M^2} dt \\
 &\quad + \frac{1}{T} \int_{(d+d_2)T}^T \frac{v_{C1} - v_{C2}}{L_2} dt \\
 \frac{dv_{C1}}{dt} &= -\frac{1}{T} \int_0^{d_1 T} \frac{i_{L2}}{C_1} dt - \frac{1}{T} \int_{dT}^{(d+d_2)T} \frac{i_{L2} - i_{L1}}{C_1} dt \\
 &\quad - \frac{1}{T} \int_{(d+d_2)T}^T \frac{i_{L2}}{C_1} dt, \\
 \frac{dv_{C2}}{dt} &= \frac{1}{T} \int_0^{d_1 T} \left(\frac{i_{L2}}{C_2} - \frac{v_{C2}}{RC_2} \right) dt - \frac{1}{T} \int_{d_1 T}^{dT} \frac{v_{C2}}{RC_2} dt \\
 &\quad + \frac{1}{T} \int_{dT}^T \left(\frac{i_{L2}}{C_2} - \frac{v_{C2}}{RC_2} \right) dt, \tag{3}
 \end{aligned}$$

According to temporal waveforms in Fig. 2, the sum of integrals in i_{L2} during intervals $(0, d_1 T)$ and (dT, T) is exactly $\overline{i_{L2}}$. Moreover, it can be assumed that $v_{C1} \simeq \overline{v_{C1}}$ and $v_{C2} \simeq \overline{v_{C2}}$ in a whole switching period. Thus, system (3) reduces to

$$\begin{aligned}
 \frac{di_{L1}}{dt} &= -\frac{Md_1 + (L_2 + M)d_2}{L_1 L_2 - M^2} \overline{v_{C1}} + \frac{M(d_1 + d_2)}{L_1 L_2 - M^2} \overline{v_{C2}} \\
 &\quad + \left[\frac{L_2(d_1 + d_2)}{L_1 L_2 - M^2} + \frac{d - d_1}{L_1} \right] V_{dc}, \\
 \frac{di_{L2}}{dt} &= \left[\frac{L_1 d_1 + (L_1 + M)d_2}{L_1 L_2 - M^2} + \frac{1 - d - d_2}{L_2} \right] \overline{v_{C1}} \\
 &\quad - \left[\frac{L_1(d_1 + d_2)}{L_1 L_2 - M^2} + \frac{1 - d - d_2}{L_2} \right] \overline{v_{C2}}
 \end{aligned}$$

$$-\frac{M(d_1 + d_2)}{L_1 L_2 - M^2} V_{dc},$$

$$\begin{aligned}
 \frac{dv_{C1}}{dt} &= -\frac{1}{TC_1} \int_{dT}^{(d+d_2)T} i_{L1} dt - \frac{1}{C_1} \overline{i_{L2}}, \\
 \frac{dv_{C2}}{dt} &= \frac{1}{C_2} \overline{i_{L2}} - \frac{1}{C_2 R} \overline{v_{C2}}. \tag{4}
 \end{aligned}$$

To accomplish the averaged model, it remains to solve the integral in i_{L1} during *Mode 3* as well as to find the intervals d_1 and d_2 as functions of the averaged variables and parameter of the circuit. As is shown in the following subsections, all of these expressions can be derived by using additional information originated in the linear variation of the currents (Fig. 2). On the one hand, the average of the currents can be written as

$$\begin{aligned}
 \overline{i_{L1}} &= \frac{Ip_{11}}{2} d + \frac{Ip_{12}}{2} (d - d_1 + d_2), \\
 \overline{i_{L2}} &= \frac{Ip_{22}}{2} (1 - d) + \frac{Ip_{21}}{2} (1 - d + d_1 - d_2), \tag{5}
 \end{aligned}$$

and, on the other hand, inductor voltages in (1) define different relations between the peak currents, which are presented in Table 2.

3.1 Current integral

According to the linear variation of the currents in Fig. 2, the solution of i_{L1} integral during *Mode 3* is

$$\int_{dT}^{(d+d_2)T} i_{L1} dt = -\frac{d_2 T}{2} Ip_{12}.$$

Now, taking into account the averaged expressions in (5), it can be seen that the peak current Ip_{12} could be written as a function of $\overline{i_{L1}}$ if an additional relation between Ip_{11} and Ip_{12} was found. Based on Table 2, that relation arises from voltage v_{L1} in *Mode 2*, i.e. $Ip_{11} = Ip_{12} - (d - d_1)TV_{dc}/L_1$. Replacing it with (5) results in

$$Ip_{12} = \frac{2L_1 \overline{i_{L1}} + d(d - d_1)TV_{dc}}{L_1(2d - d_1 + d_2)}. \tag{6}$$

Then,

$$\int_{dT}^{(d+d_2)T} i_{L1} dt = -\frac{d_2 T [2L_1 \overline{i_{L1}} + d(d - d_1)TV_{dc}]}{2L_1(2d - d_1 + d_2)}. \tag{7}$$

Table 2 Voltages in the inductors according to the linear variations of Fig. 2

<i>Mode 1</i>	$v_{L1} = L_1 \frac{Ip_{11}}{d_1 T} - M \frac{Ip_{21}}{d_1 T} = V_{dc},$ $v_{L2} = -L_2 \frac{Ip_{21}}{d_1 T} + M \frac{Ip_{11}}{d_1 T} = v_{C1} - v_{C2}$
<i>Mode 2</i>	$v_{L1} = L_1 \frac{Ip_{12} - Ip_{11}}{(d - d_1)T} = V_{dc},$ $v_{L2} = \frac{M}{L_1} v_{L1}$
<i>Mode 3</i>	$v_{L1} = -L_1 \frac{Ip_{12}}{d_2 T} + M \frac{Ip_{22}}{d_2 T} = V_{dc} - v_{C1},$ $v_{L2} = L_2 \frac{Ip_{22}}{d_2 T} - M \frac{Ip_{12}}{d_2 T} = v_{C1} - v_{C2}$
<i>Mode 4</i>	$v_{L1} = \frac{M}{L_2} v_{L2},$ $v_{L2} = -L_2 \frac{Ip_{22} - Ip_{21}}{(1 - d - d_2)T} = v_{C1} - v_{C2}$

3.2 The d_1 and d_2 constraints

Since the magnetic coupling is not perfect and the flux is continuous, inductor currents commute during intervals $d_1 T$ and $d_2 T$ (Fig. 2). None of them can be neglected as they are inherent parts of the real operation of the CBC. Now, developments to find d_1 and d_2 as functions of the averages become greatly complicated considering that the four state-space variables of the circuit are involved in that magnetic process.

First, voltage relations given in Table 2 are used to obtain an adequate solution for the whole set of peak currents, i.e. Ip_{11} , Ip_{12} , Ip_{21} and Ip_{22} . As can be observed from the table, voltages v_{L1} and v_{L2} are proportional during Modes 2 and 4. Moreover, the sum $v_{L1} + v_{L2}$ in Mode 3 also verifies the Kirchhoff voltage law, permitting to eliminate one of the state variables. This means that the whole system actually reduces to five independent equations given by

- v_{L1} and v_{L2} in Mode 1;
- v_{L1} in Mode 2;
- $v_{L1} + v_{L2}$ in Mode 3;
- v_{L1} in Mode 4.

Second, the temporal dependency of variables v_{C1} and v_{C2} is eliminated from the equations to simplify the calculations. For that propose, it is assumed again that both capacitor voltages present a ripple sufficiently small compared to their average levels. So, v_{C1} and v_{C2} adopt constant values in each operation mode, which are comparatively equal to $\overline{v_{C1}}$ and $\overline{v_{C2}}$, respectively. The solution of the set of linear equations is given in “Appendix A”.

Third, the obtained solutions are replaced into current expressions in (5). Thus, a two-dimensional polynomial sys-

tem with unknown d_1 and d_2 is defined. Taking into account that $d_2 < 1 - d$ and operating algebraically by means of a mathematical symbolic software, constraints for calculating these intervals are deduced.

3.3 Model expression

Based on integral (7) in Sect. 3.1 and the d_1 and d_2 constraints obtained according to the description in Sect. 3.2, the non-linear averaged state-space model of the CBC can be finally written as shown in (8), where P_i , with $i = 1, \dots, 8$, are polynomials up to third order in the capacitor voltage states. For simplicity, their expressions are included in “Appendix B”.

$$\begin{aligned} \frac{d\overline{i_{L1}}}{dt} &= -\frac{Md_1 + (L_2 + M)d_2}{L_1 L_2 - M^2} \overline{v_{C1}} + \frac{M(d_1 + d_2)}{L_1 L_2 - M^2} \overline{v_{C2}} \\ &\quad + \left[\frac{L_2(d_1 + d_2)}{L_1 L_2 - M^2} + \frac{d - d_1}{L_1} \right] V_{dc}, \\ \frac{d\overline{i_{L2}}}{dt} &= \left[\frac{L_1 d_1 + (L_1 + M)d_2}{L_1 L_2 - M^2} + \frac{1 - d - d_2}{L_2} \right] \overline{v_{C1}} \\ &\quad - \left[\frac{L_1(d_1 + d_2)}{L_1 L_2 - M^2} + \frac{1 - d - d_2}{L_2} \right] \overline{v_{C2}} \\ &\quad - \frac{M(d_1 + d_2)}{L_1 L_2 - M^2} V_{dc}, \\ \frac{d\overline{v_{C1}}}{dt} &= \frac{d_2}{C_1(2d - d_1 + d_2)} \overline{i_{L1}} - \frac{1}{C_1} \overline{i_{L2}} \\ &\quad + \frac{d_2 d(d - d_1)T}{2C_1 L_1(2d - d_1 + d_2)} V_{dc}, \\ \frac{d\overline{v_{C2}}}{dt} &= \frac{1}{C_2} \overline{i_{L2}} - \frac{1}{C_2 R} \overline{v_{C2}}, \\ d_1 &= \frac{P_1}{P_2} (L_1 L_2 - M^2) L_1 T d_2 \\ &\quad - \frac{2L_1}{P_2} (L_1 L_2 - M^2) (L_2 + M) (L_1 \overline{i_{L1}} + M \overline{i_{L2}}) \\ &\quad + \frac{\alpha}{P_2} (L_1 L_2 - M^2) d T V_{dc} \\ d_2 &= \frac{2(L_2 + M)T P_3 (L_1 \overline{i_{L1}} + M \overline{i_{L2}}) + d T^2 P_4 - \Delta}{2T^2 P_1 P_8}, \\ \Delta^2 &= 4P_2^2 (L_2 + M)^2 (L_1 \overline{i_{L1}} - M \overline{i_{L2}})^2 \\ &\quad - M[\alpha + L_1(L_2 + M)]T^2 \\ &\quad P_2 [4P_3 \overline{i_{L1}} - 4dL_{2M} P_6 \overline{i_{L2}} + d^2 T P_7] \\ \alpha &= M(L_1 + M) + d(L_1 L_2 - M^2). \end{aligned} \tag{8}$$

Differences with respect to the model obtained by averaging the matrices are concentrated on $d\overline{v_{C1}}/dt$. In particular, the term $d_2 \overline{i_{L1}}$ is divided by $(2d - d_1 + d_2)$ and an additional term depending on V_{dc} is defined.

Table 3 Design specifications used for simulation and experimental results

Parameters		Rate values
Power		100 W
Output voltage		200 V
Switching frequency	f_s	100 kHz
Input voltage	V_{dc}	30 V
Capacitors (ripple% < 1%)	C_1	13.7 μ F
	C_2	24 μ F
Inductors ($N_2:N_1 = 4$)	L_1 (*)	50.5 μ Hy
	L_2	808 μ Hy

(*) $\Delta i_{L1} = 3A @ V_{dc} = 30V, d = 0.5$

4 Numerical results

In the following, steady-state, time-domain and small-signal frequency-domain studies are introduced to validate the proposed averaged state-space model as well as to show the dynamical behaviour of the converter. Different scenarios obtained by varying the coupling factor, the duty cycle and the load resistance are taken into account. Parameter values are detailed in Table 3, which are derived from the design specifications of a CBC.

4.1 Steady-state response

The steady-state relation between output voltage $\overline{v_{C2}}$ and V_{dc} against duty cycle d can be obtained by solving the differential system (8) equal to zero. Algebraic operations are carried out by using a mathematical symbolic program. The relation between the voltage of capacitor C_1 and V_{dc} is also calculated to characterize the behaviour of this internal component. Results for several coupling factors and load resistances are presented in Fig. 3. In particular, Fig. 3a shows voltage ratios for $R = 400\Omega$ and three different k values. The reduction in $\overline{v_{C2}}/V_{dc}$ with the decrease of k can be observed. Indeed, the diminution of the coupling factor implies that commutation intervals of the currents i_{L1} and i_{L2} increase, reducing the output power. This condition becomes more evident for high d values because both the output current and the commutation interval naturally increase. Relation $\overline{v_{C1}}/V_{dc}$ has an opposite variation. As interval d_2T enlarges, the charge stored in C_1 rises (Fig. 2), incrementing its voltage level. Figure 3b depicts voltage relations for $k = 0.99$ and three possible load values. Within this range, changes in conversion ratios are very small compared to the great variations of R . As it occurs with k , sensitivity increases for high d values. Specific points obtained by simulating the converter of Fig. 1 in Simulink/MATLAB are superimposed verifying these results.

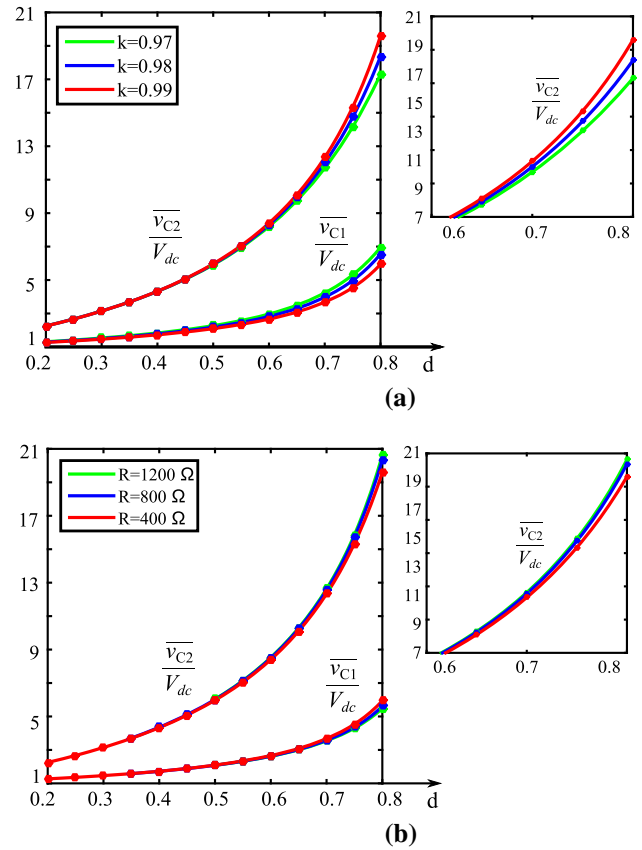


Fig. 3 Voltage ratios predicted by the averaged state-space model. **a** $R = 400\Omega$ and different coupling factors; **b** $k = 0.99$ and different load values. In both figures, (o) represents the value obtained by simulating the switched circuit

4.2 Frequency response

System (8) represents the nonlinear and large-signal dynamical behaviour of the averaged states. In order to obtain the frequency-domain response relating the output voltage $\overline{v_{C2}}$ and the control action d , differential equations in (8) have to be firstly linearized by considering small-signal variations around the operation point. So, applying the Laplace transform and operating algebraically, the control-to-output transfer function can be deduced. The generic expression is given by

$$G_d(s) = \frac{\overline{V_{C2}}(s)}{D(s)} = \frac{K_0(s + z_1)(s + z_2)}{(s^2 + 2\xi\omega_n s + \omega_n^2)(s + p_1)(s + p_2)} \tag{9}$$

Pole-zero coefficients for a duty cycle of 0.5 and different k and R values are detailed in Table 4. According to these results, $G_d(s)$ is dominated by a pair of complex poles, which strongly depends on the coupling factor. Specially, the damping factor ξ increases significantly with the decrease of k . These poles are followed by a real zero z_1 and a real pole

Table 4 Coefficients of transfer function $G_d(s)$ around a duty cycle of 0.5 and different k and R values

	$K_0 (\times 10^{10})$	z_1 rad/s	z_2 rad/s	ξ	ω_n rad/s	p_1 rad/s	p_2 rad/s ($\times 10^6$)
$R = 400\Omega$							
$k = 0.99$	-4.65518	14,863.4	-120,966	0.2345	2788.1	14,323	1.30398
$k = 0.98$	-4.58514	7733.34	-118,980	0.4503	2570.7	8696.78	1.29942
$k = 0.97$	-4.52015	5341	-117,540	0.6307	2211.7	8128.21	1.29005
$R = 800\Omega$							
$k = 0.99$	-2.45252	8883.32	-307,023	0.3054	2790.3	8976.96	1.63656
$k = 0.98$	-2.45062	4538.46	-302,590	0.6046	2570.6	5387.49	1.6261
$k = 0.97$	-2.44826	3092.51	-298,251	0.8279	2040.5	5819.93	1.61298

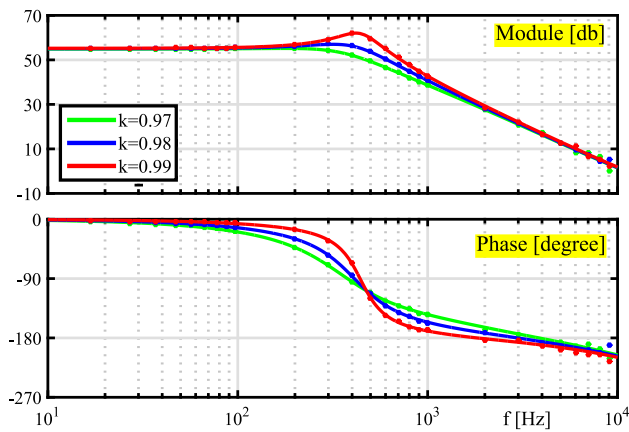


Fig. 4 Frequency response for $d = 0.5$, $R = 400\Omega$ and different coupling factors obtained by means of the averaged model. (o) measurements of the switched circuit

p_1 that separate between each other also according to k . The dynamics is completed by a non-minimum phase zero z_2 and an extra real pole p_2 at very high frequencies. When load resistance is augmented from 400Ω to 800Ω , minor changes occur at the dominant low-frequency dynamics. As inferred from the table, this parameter affects z_2 since it moves to even higher frequencies.

The Bode plots of $G_d(s)$ for $R = 400\Omega$ and the three k values considered in Table 4 are depicted in Fig. 4. It can be appreciated that module and phase change significantly in the range of 100 Hz–2 kHz around ω_n due to the strong influence of k . In particular, the quality factor $Q = 1/(2\xi)$ drops almost 10 dB even when k only decreases 2%. Simulated results obtained by injecting a small-signal frequency sweep to the converter of Fig. 1 around its steady-state operation are included in the figure (circles). Comparisons reveal the adequate behaviour of the obtained small-signal model considering this is valid up to a decade before the switching frequency. By means of the averaged system (8), other transfer functions could be evaluated.

4.3 Time response

Time responses of the inductor currents and capacitor voltages when different instantaneous changes are applied on the duty cycle for $k = 0.99$ and $R = 400\Omega$ are presented in Fig. 5. In the figures, the dark solid lines correspond to the temporal evolutions observed by the averaged state variables of model (8) while the grey lines correspond to the waveforms resulting from the simulation of the converter. For comparison, responses obtained by means of the linearization of (8) around $d = 0.5$ are included with dot-dashed lines. Moreover, the mean values of the currents provided by the simulations are superimposed with dashed white lines.

Figure 5a shows the results obtained by increasing d from 0.5 to 0.51 at $t = 0$ and then, decreasing it from 0.51 to 0.5 at $t = 0.02s$. The output voltage \bar{v}_{C2} predicted by (8) manifests an under-damping behaviour characterized by an approximate overshoot of 46% and rise and settling times of around 0.65 ms and 7ms, respectively. Responses of the averaged variables \bar{i}_{L1} , \bar{i}_{L2} and \bar{v}_{C1} are congruent with \bar{v}_{C2} , evidencing significant under-/overshoots before reaching their new steady-state values. As it can be seen, the averaged model follows appropriately the dynamical changes of the currents and voltages of the CBC converter.

Since the steps applied to d are small, almost the same responses are obtained by means of the linearized model (dot-dashed lines). In fact, characteristics of voltage \bar{v}_{C2} are in agreement with the second-order polynomial that dominates $G_d(s)$. Calculations for ξ and ω_n values given in Table 4 predict an overshoot of $100e^{(-\pi\xi/\sqrt{1-\xi^2})} = 46.82\%$, a rise time of $1.8/\omega_n = 0.6478$ ms and a settling time of $4.6/(\xi\omega_n) = 7.05$ ms [13].

Figure 5b depicts the temporal responses when d is increased from 0.5 to 0.53 at $t = 0$ and then, it decreases from 0.53 to 0.51 at $t = 0.02s$. As can be observed, changes in the duty cycle are slightly greater than those used in the previous case. However, the linearized model presents visible differences with respect to the simulations, especially in

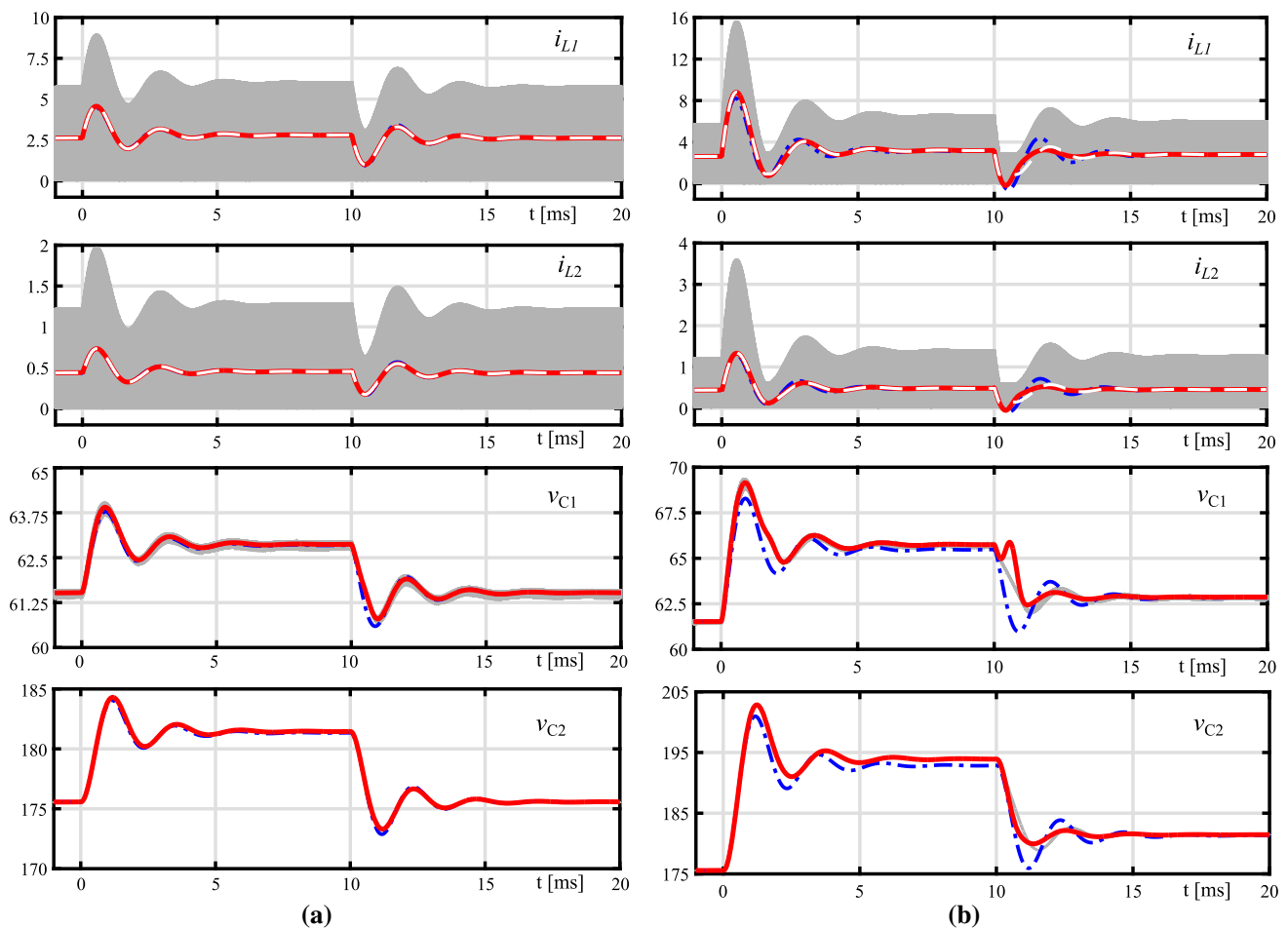


Fig. 5 Temporal responses when different steps are applied to the duty cycle. **a** d is increased from 0.5 to 0.51 at $t = 0$ s and then decreased from 0.51 to 0.5 at $t = 0.01$ s. **b** d is increased from 0.5 to 0.53 at $t = 0$ s and then decreased from 0.53 to 0.51 at $t = 0.01$ s. Dark solid

line: average values predicted by (8); Dot-dashed line: average values given by the linearization of (8) around $d = 0.5$; grey line: waveforms of the simulated circuit; white dashed line: averages calculated by the simulated currents

the output voltage. This evidences the importance of the non-linearities immersed in model (8) to follow more precisely the dynamics of the circuit.

According to the load current and the step-down applied to d , the converter can undergo a discontinuous operation mode for a few switching periods during the transient. While this occurs, the averaged model cannot predict exactly the actual behaviour of the mean currents and voltages. As noticed in Fig. 5b after the step-down at $t = 0.02$ s, averages $\overline{i_{L1}}$ and $\overline{i_{L2}}$ predicted by the model invert their sign for a short time. This condition is impossible in the converter due to the presence of the diodes. Indeed, mean currents of the circuit keep an almost constant value during approximately 1 ms while the discontinuous conduction mode is reached. Consequently, inductors act like current generators and, considering that the load current is approximately constant too during that time interval, capacitors C_1 and C_2 present a constant voltage rate.

5 Introduction of parasitic losses

Up to now, the averaged model was obtained by assuming ideal components and a coupling factor less than one. Indeed, components used to build converters usually possess parasitic capacitances and resistances that can introduce differences between physical and predicted dynamical and steady-state behaviours. Considering that parasitic capacitances of windings and semiconductors have effects at very high frequencies, only parasitic resistances are seen as critical elements in the frequency range of validity of an averaged model [13,14].

The incorporation of the resistive losses of the components into the electrical equations of the four operation modes of the converter (Table 1) increases significantly the complexity of a new averaging process. As an alternative, system (8) can be represented as the equivalent circuit shown in Fig. 6a. Capacitors C_1 and C_2 and inductors L_1 and L_2 are clearly identified,

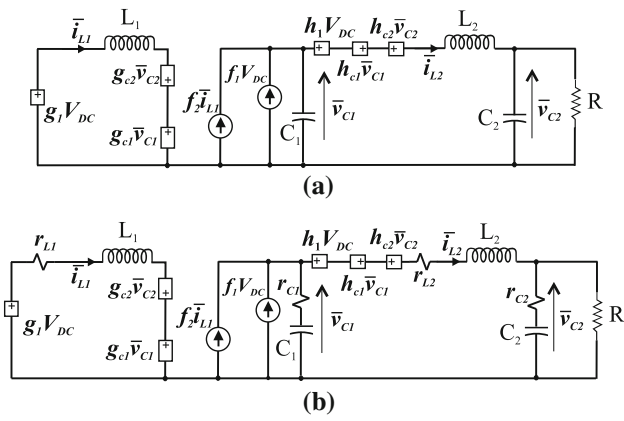


Fig. 6 Equivalent averaged circuits of the CBC. **a** Without losses; **b** with resistive losses

preserving the connections of the original switched converter. So, two stages can be defined: the input one corresponding to L_1 and the output one corresponding to L_2 . Both stages are interacting between each other by dependent voltages and currents sources, given by the coefficients

$$\begin{aligned}
 g_1 &= \frac{L_2(d_1 + d_2)}{L_1L_2 - M^2} + \frac{d - d_1}{L_1}, \\
 g_{C1} &= \frac{Md_1 + (L_2 + M)d_2}{L_1L_2 - M^2}, \\
 g_{C2} &= \frac{M(d_1 + d_2)}{L_1L_2 - M^2}, \\
 h_1 &= -\frac{M(d_1 + d_2)}{L_1L_2 - M^2}, \\
 h_{C1} &= \frac{L_1d_1 + (L_1 + M)d_2}{L_1L_2 - M^2} + \frac{1 - d - d_2}{L_2} - 1, \\
 h_{C2} &= h_{C1} - \frac{Md_2}{L_1L_2 - M^2}, \\
 f_1 &= \frac{d_2d(d - d_1)T}{2C_1L_1(2d - d_1 + d_2)}, \\
 f_2 &= \frac{d_2}{C_1(2d - d_1 + d_2)}.
 \end{aligned}$$

Then, parasitic resistances are added in series to each component of the equivalent averaged circuit, as indicated in Fig. 6b. Equivalent resistances r_{L1} and r_{L2} represent the losses associated with inductors and semiconductors of the input and output stages, respectively. Similarly, r_{C1} and r_{C2} are the equivalent series resistances (ESR) of C_1 and C_2 , respectively. The application of the Kirchhoff laws to the new circuit containing parasitic losses results in the complete averaged state-space model presented in (10). It is important to highlight that the effect of losses also reaches the time intervals d_1T and d_2T since they are calculated by means of the aver-

aged state values of the new system.

$$\begin{aligned}
 \frac{d\bar{i}_{L1}}{dt} &= \frac{1}{L_1} \left(g_1V_{dc} + g_{C1}\bar{v}_{C1} + g_{C2}\bar{v}_{C2} - r_{L1}\bar{i}_{L1} \right) \\
 \frac{d\bar{i}_{L2}}{dt} &= \frac{1}{L_2} \left(-h_1V_{dc} + h_{C1}\bar{v}_{C1} - h_{C2}\bar{v}_{C2} - r_{L2}\bar{i}_{L2} \right), \\
 \frac{d\bar{v}_{C1}}{dt} &= \frac{1}{C_1} \left(f_1V_{dc} + f_2\bar{i}_{L1} - \bar{i}_{L2} \right) + r_{C1} \left(f_2\frac{d\bar{i}_{L1}}{dt} - \frac{d\bar{i}_{L2}}{dt} \right), \\
 \frac{d\bar{v}_{C2}}{dt} &= \frac{1}{C_2} \left(\frac{R}{R+r_{C2}}\bar{i}_{L2} - \frac{1}{R+r_{C2}}\bar{v}_{C2} \right) + \frac{Rr_{C2}}{R+r_{C2}}\frac{d\bar{i}_{L2}}{dt}, \\
 d_1 &= \frac{P_1}{P_2} (L_1L_2 - M^2)L_1Td_2 \\
 &\quad - \frac{2L_1}{P_2} (L_1L_2 - M^2)(L_2 + M)(L_1\bar{i}_{L1} + M\bar{i}_{L2}) \\
 &\quad + \frac{\alpha}{P_2} (L_1L_2 - M^2)dTV_{dc} \\
 d_2 &= \frac{2(L_2 + M)TP_3(L_1\bar{i}_{L1} + M\bar{i}_{L2}) + dT^2P_4 - \Delta}{2T^2P_1P_8}, \\
 \Delta^2 &= 4P_2^2(L_2 + M)^2(L_1\bar{i}_{L1} - M\bar{i}_{L2})^2 \\
 &\quad - M[\alpha + L_1(L_2 + M)]T^2 \\
 &\quad P_2[4P_5\bar{i}_{L1} - 4dL_{2M}P_6\bar{i}_{L2} + d^2TP_7] \\
 \alpha &= M(L_1 + M) + d(L_1L_2 - M^2). \tag{10}
 \end{aligned}$$

6 Experimental test

In order to test averaged model (10) under steady-state and dynamical conditions, a prototype built in the laboratory was used. For comparison, results obtained by simulating model (8) are also taken into account. Design specifications listed in Table 3 are completed with measurements made on the circuit and its components. So, the achieved coupling factor is $k = 0.99$ and the equivalent resistances are $r_{L1} = 0.2\Omega$, $r_{L2} = 2.8\Omega$, $r_{C1} = 77m\Omega$ and $r_{C2} = 5.6m\Omega$. Moreover, the load resistance is fixed at $R = 400\Omega$.

6.1 Steady-state response

Figure 7 shows voltage conversion ratios \bar{v}_{C2}/V_{dc} and \bar{v}_{C1}/V_{dc} as a function of the duty cycle. Results given by averaged models with and without resistive losses are indicated with solid and dashed lines, respectively. As expected, parasitics reduce the gains as d is increased due to the inherent increment of the mean values of the currents. Measurements made on the prototype for specific operation points are superposed to the curves by means of circles. The maximum implemented duty cycle was $d = 0.65$ since the converter achieves the designed rate power. It can be seen that model described by (10) adjusts more precisely the steady-state levels of the experimental set-up.

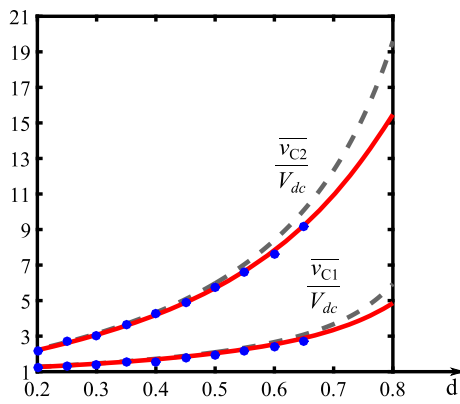


Fig. 7 Predicted voltage steady-state ratios of the CBC for $R = 400\Omega$, $k = 0.99$. Solid line: averaged model (10) including resistive losses; dashed line: model (8) without considering resistive losses; (o): measurements made on the prototype

6.2 Frequency response

Frequency-domain response of the converter is studied by means of the control-to-output-voltage transfer function. Based on the parameters of the prototype and the expression of the averaged model (10), the new transfer function around a duty cycle of 0.5 is given by

$$G_d(s) = \frac{K_0(s + z_1)(s + z_2)(s + z_3)}{(s^2 + 2\xi\omega_n s + \omega_n^2)(s + p_1)(s + p_2)} \quad (11)$$

with $K_0 = -5983.08$, $z_1 = -121,042$ rad/s, $z_2 = 14,773$ rad/s, $z_3 = 7.44048 \times 10^6$ rad/s, $\xi = 0.84267$, $\omega_n = 2822.65$ rad/s, $p_1 = 14,482.5$ rad/s, $p_2 = 1.32457 \times 10^6$ rad/s. Compared to (9) without containing resistive losses, function (11) presents an additional real zero. This singularity is located at a very high frequency, which can be actually associated with the ESR of the output capacitor since $1/C_2 r_{C2} = 7.44 \times 10^6$. Another particularity is that the real zero z_1 and the real pole p_1 approach each other, causing a practically cancellation. But, it can be mainly noticed that the parasitic losses affect the characteristics of the dominant pair of complex poles.

Figure 8 presents the Bode plots corresponding to the transfer functions with (solid line) and without (dashed line) parasitic losses. In both cases, the second-order polynomial leads to dominant responses at a natural frequency of around 450 Hz. However, the damping factor of the transfer function (11) is $\xi = 0.84266$, which is appreciably greater than that of the transfer function without losses ($\xi = 0.2348$). So, the quality factor Q drops from +6.56 dB (under-damped system) to -4.53 dB (over-damped system).

The frequency response of the prototype was measured by using a dynamic signal analyser (model Agilent 35670A), which injects a frequency sweep of small-signal magnitude around the duty cycle of the switch. Experimental results for

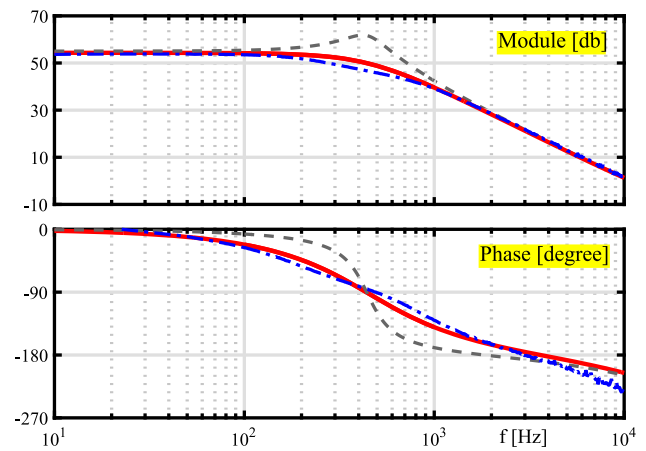


Fig. 8 Control-to-output-frequency response around $d = 0.5$ for $R = 400\Omega$ and $k = 0.99$. Solid line: averaged model with resistive losses; dashed line: averaged model without losses; dot-dashed line: response of the prototype

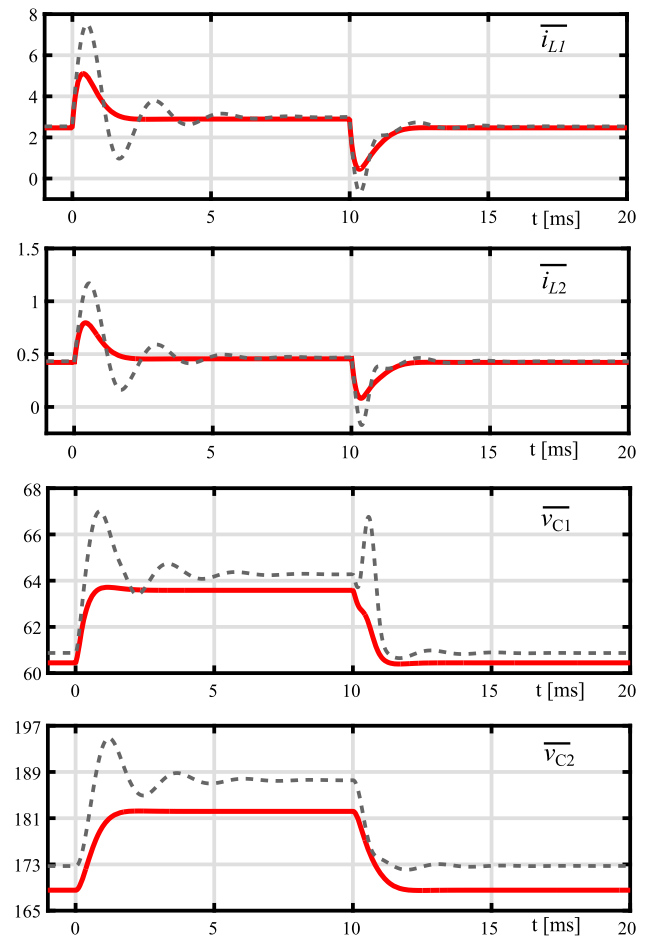


Fig. 9 Temporal responses of model (10) considering losses for $R = 400\Omega$, $k = 0.99$ and varying d from 0.495 to 0.52 and vice versa. Dashed line: model (8) without considering losses

$d = 0.5$ are indicated in Fig. 8 with a dot-dashed line. As it can be observed, system (10) follows the measurements appropriately replicating the DC-gain, magnitude and phase

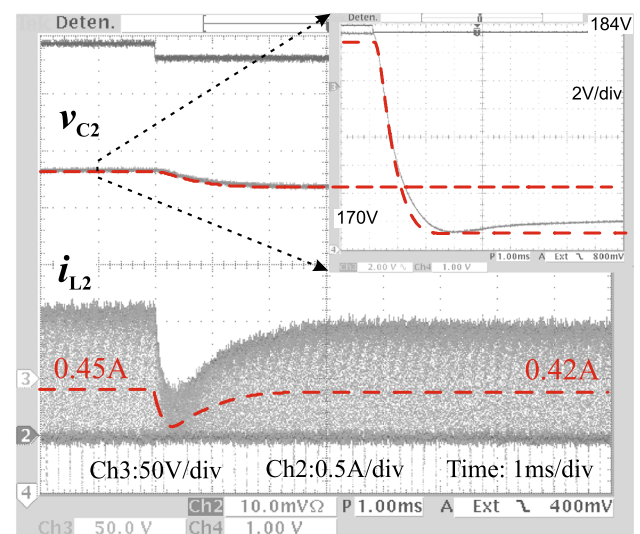
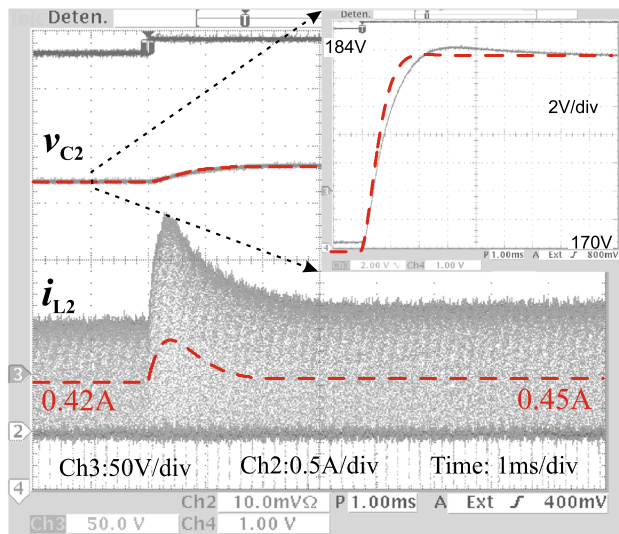
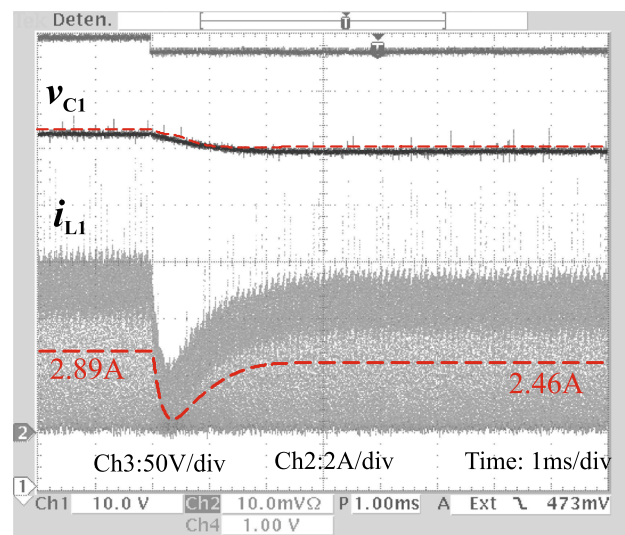
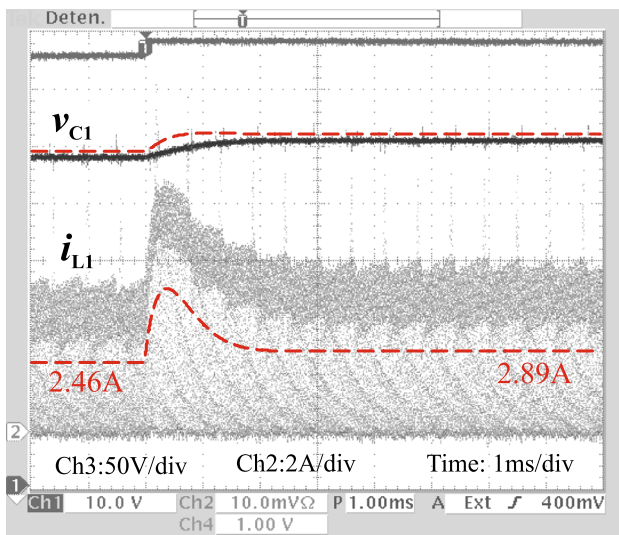


Fig. 10 Oscilloscope current and voltage waveforms when a step-up is applied to duty cycle of the prototype

Fig. 11 Oscilloscope current and voltage waveforms when a step-down is applied to duty cycle of the prototype

asymptotes, negative phase margin as well as the evident existence of an over-damped dominant response. Bode plot of the prototype shows a slightly major attenuation around 450 Hz and some minimum deviations along the phase. Differences can be attributed to normal uncertainties in the parameter values as well as to possible errors in the phase measuring, specially at frequencies close to the switching frequency f_s .

6.3 Temporal response

Time responses predicted by averaged models when the duty cycle changes from 0.495 to 0.52, and vice versa, are shown in Fig. 9. In all figures, averaged currents and voltages of system (10) are represented by solid lines while the variables predicted by (8) are indicated with dashed lines. Differences

in the steady-state levels of the voltages are in agreement with curves given in Fig. 7. With respect to the transients, model (10) always presents a notably greater damping, following the tendency of the respective second-order dominant poles. In the figure, the temporal response of v_{C2} presents an overshoot of 0.04% and rise and settling times of approximately 1.14 ms and 2 ms, respectively. The second-order system in (11) predicts responses with an overshoot of -0.73% , a rise time of 0.65 ms and a settling time of 2 ms. These deviations reveal again the effects of the nonlinearities immersed in model (10) even though the duty cycle changes seem to be small.

Figure 9 also shows that the damping introduced by the resistive losses reduces the time intervals where the converter operates in discontinuous conduction mode due to a high

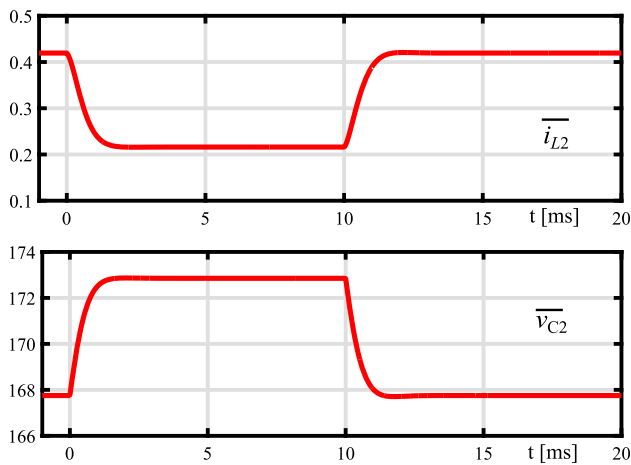


Fig. 12 Temporal responses of model (10) increasing the load resistance from 400 to 800 Ω at $t = 0$ and then reducing it from 800 to 400 Ω at $t = 0.01$ s

step-down applied on d (at $t = 0.01$ s). As shown in the previous section, the occurrence of that phenomenon can traduce into an inversion of the sign of the currents predicted by the model. Variables $\overline{i_{L1}}$ and $\overline{i_{L2}}$ obtained by (10) keep the positive sign. However, this condition is not enough to guarantee the permanent continuous conduction mode of the real converter.

Figures 10 and 11 show the oscilloscope waveforms of currents and voltages of the prototype when the duty cycle steps simulated in Fig. 9 were injected to the command of the switch S . The average values predicted by (10) are overlapped in the figures (dashed lines). The zoom-in views permit to see clearly the transients of the output voltage. In both cases, the model follows the average dynamics of the converter very appropriately.

6.4 Close-loop response

In general, the output voltage of a DC–DC converter should maintain constant irrespective of variations in the parameters, load or input voltage. Figure 12 presents the response of the output variables of the CBC model fixing $d = 0.5$ and introducing instantaneous changes to the load resistance. The R value is increased from 400 Ω to 800 Ω at $t = 0$, and then, it is decreased from 800 Ω to 400 Ω at $t = 0.01$. These results illustrate that the regulation of the CBC will not be good if the circuit operates without a control loop.

Based on the valuable understanding provided by model (10), it can be now possible to implement a feedback loop leading to an accurate and reliable regulation of the converter. As an example, the transfer function (11) is considered here to design a conventional voltage-mode controller by following classical linear tools. An integral action is mainly used to assure zero steady-state error. A gain compensator and

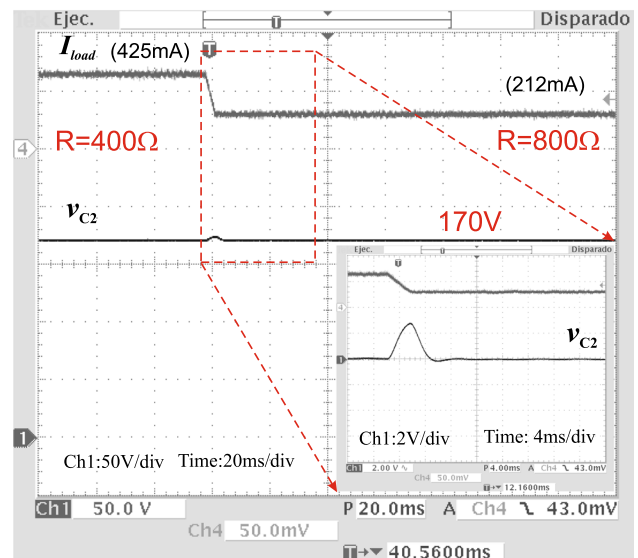
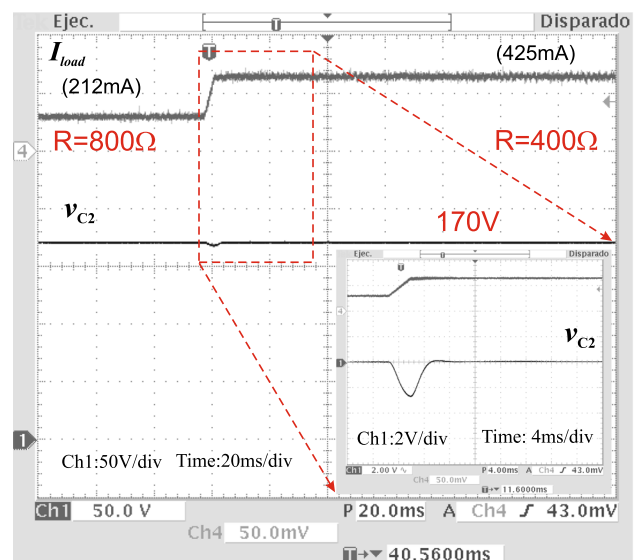


Fig. 13 Output voltage regulation of the closed-loop system under load changes

a zero-pole compensator are also added to shape the transients and to filter high frequencies. Taking into account the attenuations introduced by the PWM and sensing stages (0.016/3) and defining a closed-loop response with a bandwidth of 150 Hz, the resulting expression is given by $C(s) = 2700(s + 2800)/s(s + 30,000)$.

The performance of the closed-loop system under load changes is shown in Fig. 13. The prototype is operating with a duty cycle around 0.5 and an output voltage of 170V. Experiments in the figure correspond to R transitions from 400 Ω to 800 Ω , and vice versa, implemented by means of an electronic load (model TECH8514B). Each oscilloscope screen displays the monitor equivalent current (upper trace) and the output voltage of the CBC (lower trace). The tem-

poral response of v_{C2} can be also observed in the zoom-in views. The system keeps the regulation after the changes, and the settling time of the transients is around 5 ms, which is consistent with the closed-loop specification.

7 Conclusions

An averaged state-space model of a coupled-inductor converter has been developed in this paper. Due to the natural loss of perfect coupling and the large fluctuations of the inductor currents, special attention had to be paid to the application of the averaging technique. In fact, the differential equations of the four state variables were obtained by averaging the circuit equations for each of the operation modes over a switching period. Moreover, an algebraic process was carried out to express the current commutation intervals as a function of the averaged states and the duty cycle of the switch.

The averaged system was firstly deduced by considering ideal components. Voltage conversion ratios with respect to the duty cycle were predicted for different coupling factors and load resistances. Variations were mainly observed with the decrease of the coupling, specially for high duty cycles. Small-signal dynamical behaviours were analysed by means of the frequency-domain response of the control-to-output relation. That transfer function presents a dominant pair of complex poles accompanied by real poles and zeros at higher frequencies. Transient responses due to sudden changes in the duty cycle were also studied. Despite the nonlinearities of the model, the output voltage presents overshoots, rise and setting times consistent with the characteristics of the dominant second- order polynomial. Simulations of the converter evidence that the model follows its average dynamic very appropriately.

Then, resistive losses of the components were included to the averaged model. To handle them in a simple way, an equivalent circuit keeping the component connection of the original converter was derived. So, the equivalent loss resistances were inserted directly in series to the elements. Obtained results show that the losses mainly affect the damping of the dominant dynamical response and the steady-state values of the voltages. The performance of the averaged system with losses was tested by using a prototype. Predicted time- and frequency-domain responses were in a very good agreement with experimental measurements.

The proposed model is demonstrated to be useful for understanding and characterizing the small- and large-signal average behaviours of the converter under coupling factor variations and the existence of parasitic losses. Furthermore, it can seen as a accessible tool for approximating these parameters to their actual values as well as for designing controllers by using, for example, classical linear techniques.

Acknowledgements Authors acknowledge the financial support of SGCyT at the Universidad Nacional del Sur, Universidad Nacional de La Plata, CONICET and ANPCyT.

Appendix A

The solution of set of linear equations defined in Subsection 3.2 is given by

$$\begin{aligned}
 Ip_{11} &= \frac{d_1 T [L_2 V_{dc} - M(\overline{v_{C1}} - \overline{v_{C2}})]}{L_1 L_2 - M^2}, \\
 Ip_{12} &= \frac{dT}{L_1} V_{dc} + \frac{d_1 T M [M V_{dc} - L_1(\overline{v_{C1}} - \overline{v_{C2}})]}{L_1 (L_1 L_2 - M^2)}, \\
 Ip_{21} &= \frac{d_1 T [M V_{dc} - L_1(\overline{v_{C1}} - \overline{v_{C2}})]}{L_1 L_2 - M^2}, \\
 Ip_{22} &= \frac{d_1 M (L_1 + M) T [M V_{dc} - L_1(\overline{v_{C1}} - \overline{v_{C2}})]}{L_1 (L_2 + M) (L_1 L_2 - M^2)} \\
 &\quad + \frac{T [d(L_1 + M) V_{dc} + d_2 L_1 (V_{dc} - \overline{v_{C2}})]}{L_1 (L_2 + M)}
 \end{aligned}$$

Notice that Ip_{12} is equivalent to (6) since both expressions arise in the same set of equations (Table 2). But, additional relations given by the average of the currents are used here to find d_1 and d_2 values.

Appendix B

Considering that $L_{1M} = L_1 + M$, $L_{2M} = L_2 + M$, $L_p = L_1 + L_2$, $L_n = L_1 - L_2$, $L_d = dL_2 + M$ and $L_\alpha = M[\alpha + L_1(L_2 + M)]$, the polynomials that permit to calculate d_1 and d_2 as a function of the average state-space variables are

$$\begin{aligned}
 P_1 &= L_d V_{dc} - (1 - d) M \overline{v_{C2}}, \\
 P_2 &= L_\alpha T [-M V_{dc} + L_1(\overline{v_{C1}} - \overline{v_{C2}})], \\
 P_3 &= [(1 - d) M^2 L_p + 2L_1^2 L_2 L_d] V_{dc} \\
 &\quad - L_1 L_\alpha \overline{v_{C1}} + L_1 (3L_\alpha - 4L_1 M L_{2M}) \overline{v_{C2}}, \\
 P_4 &= \{(1 - d) M (M^4 + L_2 L_\alpha) \\
 &\quad - L_1 L_2 L_d [3(1 - d) M^2 + 2L_1 L_d]\} V_{dc}^2 \\
 &\quad + L_1 L_\alpha (2L_d - L_{2M}) V_{dc} \overline{v_{C1}} \\
 &\quad + 2(1 - d) L_1 M L_\alpha \overline{v_{C2}} (\overline{v_{C2}} - \overline{v_{C1}}) \\
 &\quad + L_1 \{L_{2M} L_\alpha + 4M [(1 - d)^2 M^2 L_2 \\
 &\quad - d L_1 L_2 (L_d + M) - L_1 M^2]\} V_{dc} \overline{v_{C2}}, \\
 P_5 &= -[2M L_{1M} L_p + 2d(L_2 - L_d)(L_1^2 L_2 + M^3) \\
 &\quad + d L_1 M (L_2^2 - M^2)] V_{dc}^2 \\
 &\quad + L_1 [2M L_\alpha + 2d L_2 (1 - d) M^2 \\
 &\quad - d L_1 (2d L_2 M + L_2^2 + 3M^2)] V_{dc} \overline{v_{C1}} \\
 &\quad + d L_1^2 M^2 V_{dc} \overline{v_{C2}}
 \end{aligned}$$

$$\begin{aligned}
& +\{L_1^2 L_2[(1-2d)L_d + M(1-8d+4d^2)] \\
& -2(1-d)M[ML_1(2L_1+3L_d) - L_\alpha]\}V_{dc}\overline{v_{C2}} \\
& -2(1-d)L_1\{M[(1-d)ML_{1M} + L_1L_{2M}]\overline{v_{C1}} \\
& -[L_\alpha - L_1ML_d + (1-d)M^3]\overline{v_{C2}}\}\overline{v_{C2}},
\end{aligned}$$

$$\begin{aligned}
P_6 & = (2L_1L_2L_d + M^2L_{2M})V_{dc}^2 \\
& -L_1M(L_{2M} + 2L_d)V_{dc}\overline{v_{C1}} \\
& -L_1M(L_{2M} - 4L_d)V_{dc}\overline{v_{C2}} \\
& -2(1-d)L_1M^2\overline{v_{C2}}(\overline{v_{C2}} - \overline{v_{C1}}),
\end{aligned}$$

$$\begin{aligned}
P_7 & = -M(L_{2M} - 2dL_2)^2V_{dc}^3 \\
& +[L_1L_{2M}^2 - 4(1-d)M^2L_d]V_{dc}^2\overline{v_{C1}} \\
& +4(1-d)(L_\alpha - L_1ML_{2M} - 2L_1ML_d)V_{dc}\overline{v_{C2}}\overline{v_{C1}} \\
& -4(1-d)(L_\alpha - 3L_1ML_d)V_{dc}\overline{v_{C2}}^2 \\
& -(L_{2M} - 2L_d)[4(1-d)M^2 \\
& +L_1(L_{2M} - 2L_d)]V_{dc}^2\overline{v_{C2}} \\
& +4(1-d)^2L_1M^2\overline{v_{C2}}^2(\overline{v_{C1}} - \overline{v_{C2}}),
\end{aligned}$$

$$\begin{aligned}
P_8 & = (ML_{1M} + dL_n)[L_pV_{dc} + L_1M(2\overline{v_{C2}} - \overline{v_{C1}})] \\
& -L_1^2ML_{2M}\overline{v_{C1}}.
\end{aligned}$$

References

- Lessa TF, de Castro PD, Josias de Paula W, de Sousa Oliveira JD (2015) Survey on non-isolated high-voltage step-up dc–dc topologies based on the boost converter. *IET Power Electron* 8(10):2044–2057
- Forouzesh M, Siwakoti YP, Gorji SA, Blaabjerg F, Lehman B (2017) Step-up DC–DC converters: a comprehensive review of voltage-boosting techniques, topologies and applications. *IEEE Trans Power Electron* 32(12):9143–9178
- Hu X, Gong C (2014) A high voltage gain dc–dc converter integrating coupled-inductor and diode-capacitor techniques. *IEEE Trans Power Electron* 29(2):789–800
- Ajami A, Ardi H, Farakhor A (2015) A novel high step-up DC/DC converter based on integrating coupled inductor and switched-capacitor techniques for renewable energy applications. *IEEE Trans Power Electron* 30(8):4255–4263
- Alencar Freitas AA, Lessa Tofoli F, Mineiro Sá Júnior E, Daher S, Antunes FLM (2015) High-voltage gain dc–dc boost converter with coupled inductors for photovoltaic systems. *IET Power Electron* 8(10):1885–1892
- Patidar K, Umarikar AC (2016) A step-up PWM DC–DC converter for renewable energy applications. *Int J Circuit Theory Appl* 44(4):817–832
- Sri Revathi B, Prabhakar M (2018) Modular high-gain DC-DC converter for renewable energy microgrids. *Electr Eng*. <https://doi.org/10.1007/s00202-017-0673-5>
- Van de Sype DM, De Gussem K, Renders B, Van den Bossche AP, Melkebeek JA (2005) A single switch boost converter with high conversion ratio. *Proc IEEE Appl Power Electron Conf (APEC)* 3:1581–1587
- Zhao Q, Lee FC (2003) High-efficiency, high step-up dc–dc converters. *IEEE Trans Power Electron* 18(1):65–73
- Berkovich Y, Axelrod B (2011) Switched-coupled inductor cell for DC–DC converters with very large conversion ratio. *IET Power Electron* 4(3):309–315
- Chen S-M, Lao M-L, Hsieh Y-H, Liang T-J, Chen K-H (2015) A novel switched-coupled-inductor dc–dc step-up converter and its derivatives. *IEEE Trans Ind Appl* 51(1):309–314
- Nguyen TV, Petit P, Aillerie M, Salame Ch, Charles J-P (2015) Efficiency of magnetic coupled boost DC–DC converters mainly dedicated to renewable energy systems: influence of the coupling factor. *Int J Circuit Theory Appl* 43(8):1042–1062
- Erickson RW, Maksimovic D (2004) *Fundamentals of power electronics*. Springer, New York
- Kazimierczuk MK (2008) *Pulse-width modulated DC–DC power converters*. Wiley, Chichester
- Forouzesh M, Siwakoti YP, Blaabjerg F, Hasanpour S (2016) Small-signal modeling and comprehensive analysis of magnetically coupled impedance-source converters. *IEEE Trans Power Electron* 31(11):7621–7641
- Ayachit A, Siwakoti YP, Galigekere VP, Kazimierczuk MK, Blaabjerg F (2018) Steady-state and small-signal analysis of A-source converter. *IEEE Trans Power Electron* 33(8):7118–7131
- Chan C-Y, Chincholkar SH, Jiang W (2017) Adaptive current-mode control of a high step-up DC–DC converter. *IEEE Trans Power Electron* 32(9):7297–7305
- Leyva-Ramos J, Mota-Varona R, Ortiz-Lopez MG, Diaz-Saldierna LH, Langarica-Cordoba D (2017) Control strategy of a quadratic boost converter with voltage multiplier cell for high-voltage gain. *IEEE J Emerg Sel Top Power Electron* 05(4):1761–1770
- Sun J, Mitchell DM, Gruel MF, Krein PT, Bass RM (2001) Averaged modeling of PWM converters operating in discontinuous conduction mode. *IEEE Trans Power Electron* 16(4):482–492
- Davoudi A, Jatskevich J (2006) Numerical state-space averaged-value modeling of PWM DC–DC converters operating in DCM and CCM. *IEEE Trans Power Electron* 21(4):1003–1012
- Dwari S, Jayawant S, Beechner T et al (2006) Dynamics characterization of coupled-inductor boost dc–dc converters. In: *Proceedings IEEE workshop control and modelling for power electronics (COMPEL)*, pp 264–269
- Krein PT, Bentsman J, Bass RM, Lesieutre BC (1990) On the use of averaging for the analysis of power electronic systems. *IEEE Trans Power Electron* 5(2):182–190
- D'Amico MB, González SA (2017) A small-signal averaged model of a coupled-inductor boost converter. In: *Proceedings IEEE Latin American symposium on circuits and systems (LASCAS 2017)*

Publisher's Note Springer Nature remains neutral with regard to jurisdictional claims in published maps and institutional affiliations.